

Article

# Development of Visible-Light-Driven Rh–TiO<sub>2</sub>–CeO<sub>2</sub> Hybrid Photocatalysts for Hydrogen Production

Jong-Wook Hong 

Department of Chemistry and Energy Harvest-Storage Research Center (EHSRC), University of Ulsan, Ulsan 44776, Korea; jwhong@ulsan.ac.kr; Tel.: +82-52-712-8013

**Abstract:** Visible-light-driven hydrogen production through photocatalysis has attracted enormous interest owing to its great potential to address energy and environmental issues. However, photocatalysis possesses several limitations to overcome for practical applications, such as low light absorption efficiency, rapid charge recombination, and poor stability of photocatalysts. Here, the preparation of efficient noble metal–semiconductor hybrid photocatalysts for photocatalytic hydrogen production is presented. The prepared ternary Rh–TiO<sub>2</sub>–CeO<sub>2</sub> hybrid photocatalysts exhibited excellent photocatalytic performance toward the hydrogen production reaction compared with their counterparts, ascribed to the synergistic combination of Rh, TiO<sub>2</sub>, and CeO<sub>2</sub>.

**Keywords:** metal–semiconductor hybrids; hydrogen production reaction; photocatalysis; ternary nanostructure



**Citation:** Hong, J.-W. Development of Visible-Light-Driven Rh–TiO<sub>2</sub>–CeO<sub>2</sub> Hybrid Photocatalysts for Hydrogen Production. *Catalysts* **2021**, *11*, 848. <https://doi.org/10.3390/catal11070848>

Academic Editors: Chung-Shin Yuan and Chung-Hsuang Hung

Received: 16 June 2021

Accepted: 14 July 2021

Published: 15 July 2021

**Publisher's Note:** MDPI stays neutral with regard to jurisdictional claims in published maps and institutional affiliations.



**Copyright:** © 2021 by the author. Licensee MDPI, Basel, Switzerland. This article is an open access article distributed under the terms and conditions of the Creative Commons Attribution (CC BY) license (<https://creativecommons.org/licenses/by/4.0/>).

## 1. Introduction

The increasing energy demand of modern society promotes enormous research endeavors on exploiting renewable and carbon-free energy sources, among which solar energy is recognized to be a promising candidate [1–4]. The massive utilization of fossil and nuclear fuels represents serious environmental threats such as, pollutant emissions, and waste formation [1], whereas, as an attractive strategy to utilize solar energy, the production of hydrogen by solar energy has emerged as a promising strategy and can generate clean hydrogen fuel, which can be used for many applications such as industrial hydrogen reactions and fuel cells [5–10]. Among various materials, semiconductors, such as TiO<sub>2</sub> [11], ZnO [12], InP [7], Cu<sub>2</sub>O [5], CdS [13], and CeO<sub>2</sub> [14], have been considered as representative photocatalysts for hydrogen production by water splitting owing to their appropriate band structures for water reduction/oxidation, low cost, and high tolerance for photostability. However, single-component semiconductor photocatalysts exhibit significant limitations for practical application owing to their low photocatalytic efficiency arising from a limited light absorption window and fast electron–hole recombination [15–18].

Semiconductor hybrids including noble metal nanocrystals (NCs) with broad size-distributions have attracted considerable attention owing to their unique properties compared with bulk catalysts [19,20]. Among a myriad of nanostructures, nano-sized semiconductor photocatalysts, incorporating noble metal NCs with small sizes and high distributions, exhibit great potential for various photocatalytic reactions arising from their maximum atom-utilization efficiency, unique electronic structure, and abundance of low-coordinated surface atoms in the noble metal nanostructures. Based on recent developments for preparing nano-sized semiconductor photocatalysts, various approaches have recently been developed to increase the conversion efficiency of solar energy into hydrogen, such as surface atom control, metal and/or non-metal elemental doping, defect formation, and morphology control [21]. Of these many strategies, the preparation of photocatalysts by depositing small-sized noble metal nanostructures on binary semiconductors is one of the most promising approaches for boosting photocatalytic performance [4,22,23].

The formation of the Schottky junction at interfaces between noble metals and semiconductors can endow efficient extraction of photogenerated charges, thereby suppressing the recombination of charge carriers [15]. In particular, since many unsaturated surface atoms that are more active for hydrogen production reactions consist of small-sized noble metal nanostructures compared with bulk material, they can effectively promote hydrogen production [24]. In addition, photocatalysts composed of noble metal nanostructures with small sizes provide effective cost reduction. On the other hand, combining two different types of semiconductors is a promising strategy for boosting photocatalytic performance [25]. Unlike single-component semiconductors, semiconductors composed of two different semiconductors with complementary band structures can promote the efficiency of solar energy absorption. In addition, precisely controlled conduction band (CB) and valence band (VB) alignment of semiconductor photocatalysts can increase the efficiency of charge separation and migration, resulting in the suppression of electron–hole charge recombination [26–28]. Therefore, coupling two types of semiconductors with different band structures can further improve photocatalytic performance.

Herein, ternary Rh–TiO<sub>2</sub>–CeO<sub>2</sub> hybrid photocatalysts containing Rh NCs with a diameter of less than 4 nm to achieve synergistic advantages by a combination of binary semiconductors and small-sized noble metal were prepared. For the preparation of ternary Rh–TiO<sub>2</sub>–CeO<sub>2</sub> hybrid photocatalysts, CeO<sub>2</sub> and Rh domains were grown on the TiO<sub>2</sub> powder dispersed in an aqueous mixture including urea. CeO<sub>2</sub> can absorb light with a longer wavelength compared to TiO<sub>2</sub> due to its smaller band gap energy (2.85 eV) than that of TiO<sub>2</sub> (3.22 eV) [29]. Furthermore, since CB and VB edges of CeO<sub>2</sub> are more negative than those of TiO<sub>2</sub>, photo-induced electrons and holes can be efficiently accumulated in CB and TiO<sub>2</sub> and VB of CeO<sub>2</sub>, respectively, which can lead to the retardation of electron–hole charge recombination. The Rh NCs can effectively capture the electrons from the semiconductor and promote the reduction reaction [30]. Owing to synergistic effects by ternary compositions, the Rh–TiO<sub>2</sub>–CeO<sub>2</sub> hybrid photocatalysts exhibited superior photocatalytic activity for hydrogen production compared to Rh–TiO<sub>2</sub> hybrids and TiO<sub>2</sub> photocatalysts.

## 2. Results and Discussion

Rh–TiO<sub>2</sub>–CeO<sub>2</sub> and Rh–TiO<sub>2</sub> hybrid photocatalysts were prepared by seed-mediated methods growing Rh and CeO<sub>2</sub> on as-prepared bulk anatase TiO<sub>2</sub>. The crystalline and compositional features of the Rh–TiO<sub>2</sub>–CeO<sub>2</sub> hybrid, Rh–TiO<sub>2</sub> hybrid, and TiO<sub>2</sub> photocatalysts were measured using X-ray diffraction (XRD) measurement (Figure 1). All samples showed typical diffraction peaks of anatase TiO<sub>2</sub>, which signifies the preservation of the crystal structure of anatase TiO<sub>2</sub> during the growth of CeO<sub>2</sub> and Rh. The XRD patterns for the Rh–TiO<sub>2</sub>–CeO<sub>2</sub> hybrid photocatalysts showed inherent peaks corresponding to face-centered cubic (fcc) CeO<sub>2</sub>. The diffraction patterns of inherent Rh were not observed due to its low content in both Rh–TiO<sub>2</sub>–CeO<sub>2</sub> and Rh–TiO<sub>2</sub> hybrid photocatalysts. X-ray photoelectron spectroscopy (XPS) measurements for the Ti 2p, Rh 3d, and Ce 3d core levels of the Rh–TiO<sub>2</sub>–CeO<sub>2</sub> hybrid, Rh–TiO<sub>2</sub> hybrid, and TiO<sub>2</sub> photocatalysts were performed, indicating the successful formation of Rh–TiO<sub>2</sub>–CeO<sub>2</sub> hybrid photocatalysts (Figure 2). In XPS spectra, the Ti 2p binding energies of the Rh–TiO<sub>2</sub>–CeO<sub>2</sub> and Rh–TiO<sub>2</sub> hybrid photocatalysts showed higher values than that of TiO<sub>2</sub> photocatalysts. For instance, the Ti 2p<sub>3/2</sub> binding energies of the Rh–TiO<sub>2</sub>–CeO<sub>2</sub> hybrid, Rh–TiO<sub>2</sub> hybrid, and TiO<sub>2</sub> photocatalysts are 458.73, 458.72, and 458.39 eV, respectively (Figure 2a,c,e). The intimate contact of constituent elements for the Rh–TiO<sub>2</sub>–CeO<sub>2</sub> and Rh–TiO<sub>2</sub> hybrid photocatalysts can account for these changes in electronic structure.

To further investigate the formation of Rh NCs and the morphology of the products, transmission electron microscopy (TEM) images of the Rh–TiO<sub>2</sub>–CeO<sub>2</sub> hybrid, Rh–TiO<sub>2</sub> hybrid, and TiO<sub>2</sub> photocatalysts were obtained. Representative TEM images of the prepared samples are shown in Figure 3. Figure 3a,b show that pure TiO<sub>2</sub> possesses smooth surfaces. Compared with pure TiO<sub>2</sub>, Rh–TiO<sub>2</sub> hybrid photocatalysts showed the formation of highly distributed Rh NCs (3.1 ± 0.4 nm) on bulk TiO<sub>2</sub> (Figure 3c,d). Rh–TiO<sub>2</sub>–CeO<sub>2</sub> hybrid

photocatalysts also possessed small-sized Rh NCs with an average diameter of  $3.8 \pm 0.5$  nm and CeO<sub>2</sub> nanostructures distributed on the bulk TiO<sub>2</sub> (Figure 3e–g). The high-resolution TEM (HR-TEM) image of the Rh–TiO<sub>2</sub>–CeO<sub>2</sub> hybrid photocatalysts indicates that the d-spacing for adjacent lattice fringes in the NCs was 2.2 Å, which matches well with that of the (111) planes of Rh (Figure 3h) [31].

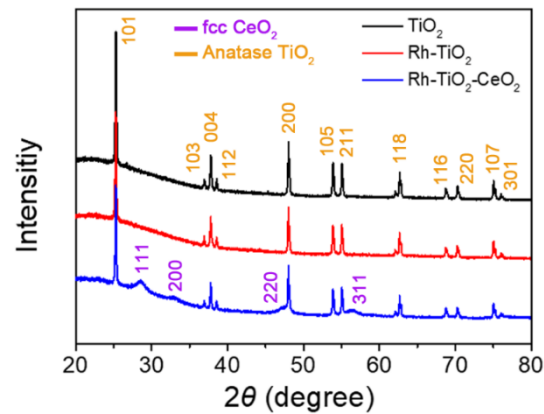


Figure 1. XRD patterns of the Rh–TiO<sub>2</sub>–CeO<sub>2</sub> hybrid, Rh–TiO<sub>2</sub> hybrid, and TiO<sub>2</sub> photocatalysts.

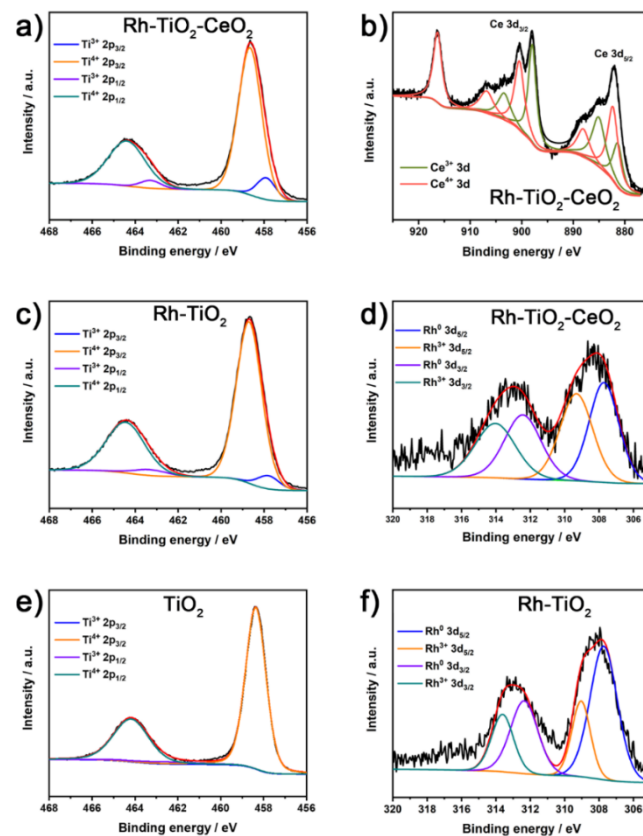
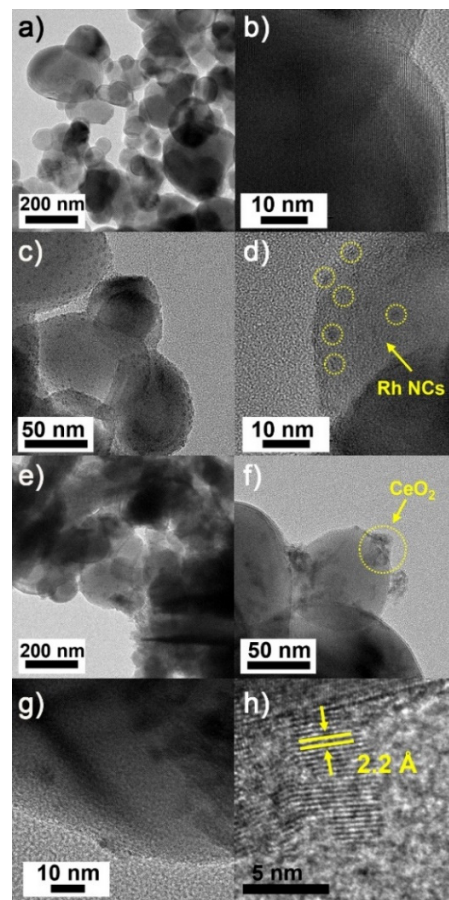
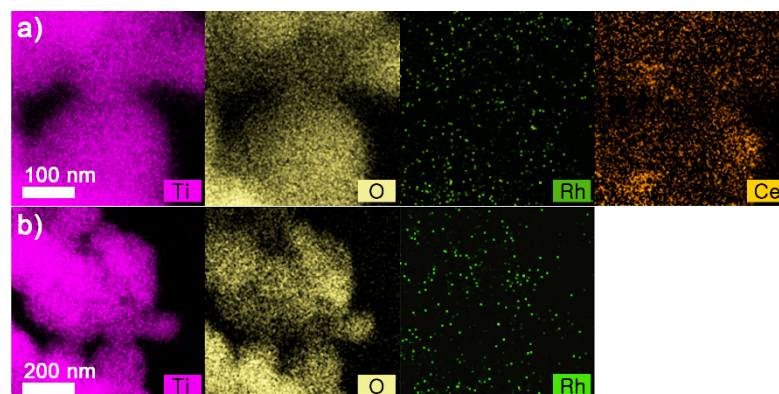


Figure 2. XPS spectra of (a,c,e) Ti 2p, (b) Ce 3d, and (d,f) Rh 3d for different photocatalysts.



**Figure 3.** TEM images of (a,b)  $\text{TiO}_2$ , (c,d)  $\text{Rh-TiO}_2$  hybrid, and (e–g)  $\text{Rh-TiO}_2\text{-CeO}_2$  hybrid photocatalysts. (h) A high-resolution TEM image focused on Rh NC in  $\text{Rh-TiO}_2\text{-CeO}_2$  hybrid photocatalysts.

To further verify the formation of  $\text{Rh-TiO}_2\text{-CeO}_2$  and  $\text{Rh-TiO}_2$  hybrid photocatalysts, the compositional structure of the  $\text{Rh-TiO}_2\text{-CeO}_2$  and  $\text{Rh-TiO}_2$  hybrid photocatalysts was investigated by elemental mapping images for Rh, Ti, Ce, and O (Figure 4). Figure 4a shows that Rh and Ce signals were highly distributed on the bulk  $\text{TiO}_2$ . In addition, the formation of  $\text{Rh-TiO}_2$  hybrid photocatalysts was verified through Rh signals observed on bulk  $\text{TiO}_2$  in the elemental mapping images (Figure 4b). The Rh/Ti/Ce and Rh/Ti atomic ratios of the  $\text{Rh-TiO}_2\text{-CeO}_2$  and  $\text{Rh-TiO}_2$  hybrid photocatalysts determined by energy dispersive X-ray spectroscopy (EDS) measurement were 0.3/87.2/12.5 and 0.5/99.5, respectively. In addition, the Rh/Ti/Ce atomic ratio of the surface for the  $\text{Rh-TiO}_2\text{-CeO}_2$  hybrid photocatalysts was 4.2/31.1/64.7 obtained from XPS measurement.



**Figure 4.** Elemental mapping images of (a)  $\text{Rh-TiO}_2\text{-CeO}_2$  and (b)  $\text{Rh-TiO}_2$  hybrid photocatalysts.

The UV–Vis diffuse reflectance spectroscopy (DRS) of Rh–TiO<sub>2</sub>–CeO<sub>2</sub> hybrids, Rh–TiO<sub>2</sub> hybrids, and TiO<sub>2</sub> photocatalysts was obtained to estimate the optical properties yielded upon the combination of Rh NPs, TiO<sub>2</sub>, and CeO<sub>2</sub> domains. As expected, TiO<sub>2</sub> absorbed only UV light due to its band gap of 3.22 eV (Figure 5a,d). In contrast, although the Rh–TiO<sub>2</sub>–CeO<sub>2</sub> hybrid photocatalysts also showed similar band gaps to the Rh–TiO<sub>2</sub> hybrid and TiO<sub>2</sub> photocatalyst (Figure 5b–d), they exhibited visible light absorption at wavelengths longer than 400 nm (Figure 5a). The slightly extended light absorption of the Rh–TiO<sub>2</sub>–CeO<sub>2</sub> hybrid photocatalysts can be attributed to the incorporation of CeO<sub>2</sub> and Rh domains into TiO<sub>2</sub>, which can yield enhanced solar energy conversion efficiency for Rh–TiO<sub>2</sub>–CeO<sub>2</sub> hybrid photocatalysts. The VB XPS pattern of Rh–TiO<sub>2</sub>–CeO<sub>2</sub> hybrid photocatalysts shows the onset at 2.58 eV.

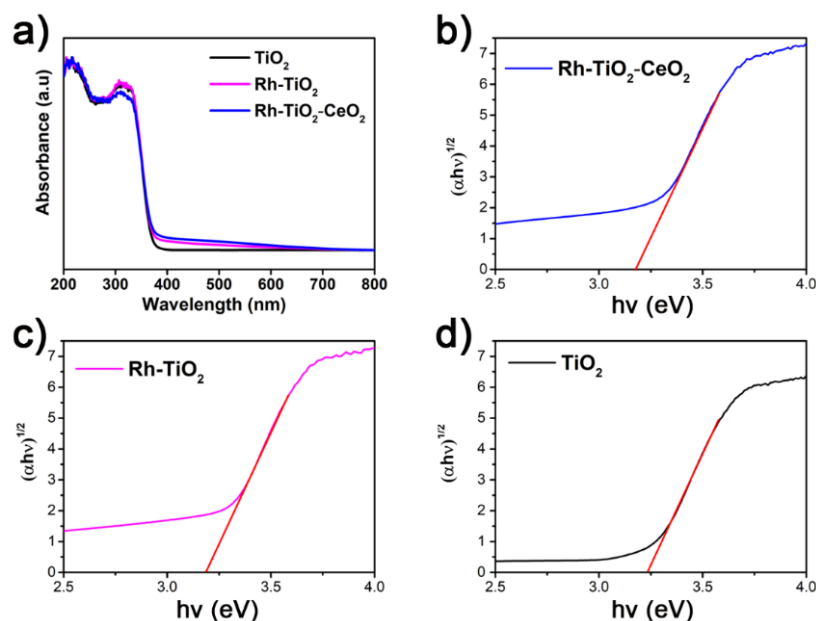


**Figure 5.** UV–Vis DRS of (a) Rh–TiO<sub>2</sub>–CeO<sub>2</sub> hybrid, Rh–TiO<sub>2</sub> hybrid, and TiO<sub>2</sub> photocatalysts and corresponding plots of the  $(\alpha h\nu)^{0.5}$  versus photon energy ( $h\nu$ ) for (b) Rh–TiO<sub>2</sub>–CeO<sub>2</sub> hybrid, (c) Rh–TiO<sub>2</sub> hybrid, and (d) TiO<sub>2</sub> photocatalysts.

The band structure of Rh–TiO<sub>2</sub>–CeO<sub>2</sub> hybrid photocatalysts was constructed based on the results of the UV–Vis DRS and VB XPS of Rh–TiO<sub>2</sub>–CeO<sub>2</sub> hybrid photocatalysts (Figure 6). Photo-induced holes in the VB of the TiO<sub>2</sub> domain transfer to the VB of the CeO<sub>2</sub> domain due to their more positive potential (Process 1 in Figure 6). Meanwhile, photo-induced electrons are accumulated in the CB of the TiO<sub>2</sub> domain through two pathways, such as the transfer of photo-induced electrons from the CB of the CeO<sub>2</sub> domain and the formation of electrons in the CB of the TiO<sub>2</sub> domain (Process 2 in Figure 6). The electrons in the CB of TiO<sub>2</sub> can migrate to Rh NCs, which leads to the production of hydrogen through a reduction reaction (Process 3 in Figure 6).

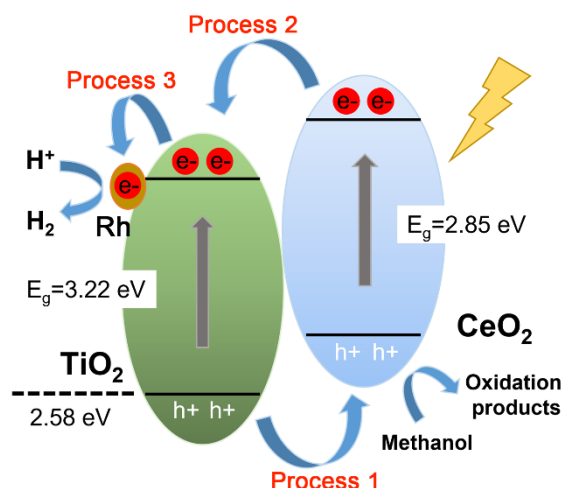


**Figure 6.** The schematic diagram of photocatalytic hydrogen production over Rh-TiO<sub>2</sub>-CeO<sub>2</sub> hybrid photocatalysts under irradiation.

To verify the advantages of the ternary Rh-TiO<sub>2</sub>-CeO<sub>2</sub> hybrid photocatalysts for photocatalytic hydrogen production, the amounts of hydrogen evolved by the Rh-TiO<sub>2</sub>-CeO<sub>2</sub> hybrid, Rh-TiO<sub>2</sub> hybrid, and TiO<sub>2</sub> photocatalysts during irradiation were measured using GC measurement. The photocatalytic hydrogen production reaction was performed under visible light irradiation ( $\lambda > 400$  nm) in a methanol/water mixture ( $v/v = 1/3$ ), in which methanol was used as a hole scavenger. Figure 7a,b show the amounts of hydrogen evolved of the Rh-TiO<sub>2</sub>-CeO<sub>2</sub> hybrid, Rh-TiO<sub>2</sub> hybrid, and TiO<sub>2</sub> photocatalysts during photocatalysis and corresponding hydrogen production rates. Apparently, the photocatalytic activity of the photocatalysts was dependent on their constituents. Noticeably, the Rh-TiO<sub>2</sub>-CeO<sub>2</sub> hybrid photocatalysts exhibited the most remarkable photocatalytic activity for hydrogen production among the different photocatalysts (Figure 7a,b), demonstrating that the formation of ternary hybrid photocatalysts constructed with two different TiO<sub>2</sub> and CeO<sub>2</sub> semiconductors and Rh NCs can lead to notable solar energy conversion efficiency. The hydrogen production rates of the Rh-TiO<sub>2</sub>-CeO<sub>2</sub> hybrid, Rh-TiO<sub>2</sub> hybrid, and TiO<sub>2</sub> photocatalysts were 48.3, 25.6, and 5.8  $\mu\text{mol g}^{-1} \text{h}^{-1}$ , respectively, which signifies that the hydrogen production rate of the Rh-TiO<sub>2</sub>-CeO<sub>2</sub> hybrid photocatalysts was 1.9 and 8.3-fold larger than those of the Rh-TiO<sub>2</sub> hybrid and TiO<sub>2</sub> photocatalysts, respectively (Figure 7b). The higher photocatalytic activity of the Rh-TiO<sub>2</sub>-CeO<sub>2</sub> hybrid photocatalysts can be attributed to efficient electron and hole transfer between interfaces of TiO<sub>2</sub>/CeO<sub>2</sub>, the efficient co-catalyst effect by Rh NCs, and enhanced visible light absorption capabilities. Based on the band structure of Rh-TiO<sub>2</sub>-CeO<sub>2</sub> hybrid photocatalysts (Figure 6), photo-induced electrons formed in CeO<sub>2</sub> migrate to the CB of TiO<sub>2</sub>, whereas photo-induced holes are accumulated in the VB of CeO<sub>2</sub>, resulting in efficient charge separation. The efficient electron and hole transfer in the Rh-TiO<sub>2</sub>-CeO<sub>2</sub> hybrid photocatalysts can suppress the charge recombination, which can effectively promote photocatalytic hydrogen production. Furthermore, Rh NCs can not only efficiently capture the electrons from both TiO<sub>2</sub> and CeO<sub>2</sub>, but also encourage the reduction reactions for producing hydrogen [29]. Taken together, the efficient photocatalytic performance of the Rh-TiO<sub>2</sub>-CeO<sub>2</sub> hybrid photocatalysts compared to the Rh-TiO<sub>2</sub> hybrid and TiO<sub>2</sub> photocatalysts can be attributed to positive synergistic effects upon combining Rh, TiO<sub>2</sub>, and CeO<sub>2</sub>. The hydrogen production activity of the Rh-TiO<sub>2</sub>-CeO<sub>2</sub> hybrid photocatalysts was compared with those of recent TiO<sub>2</sub> or CeO<sub>2</sub>-based photocatalysts (Table 1).

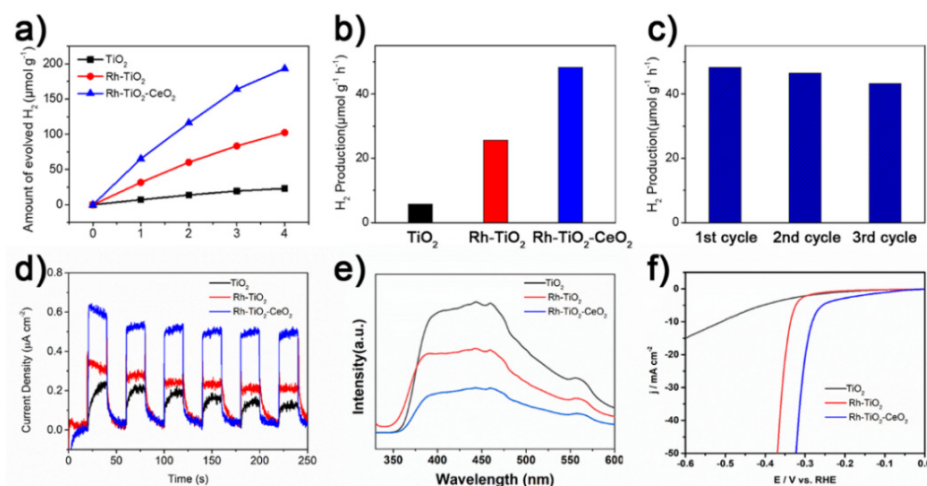


**Figure 7.** (a) Amount of evolved hydrogen during photocatalysis with different photocatalysts under visible light irradiation ( $\lambda > 400$  nm) and (b) the corresponding hydrogen production rates. (c) Recyclability of the Rh-TiO<sub>2</sub>-CeO<sub>2</sub> hybrid photocatalysts for photocatalytic hydrogen production. Each photocatalysis cycle was conducted for 4 h. (d) Photocurrents, (e) PL, and (f) HER of different photocatalysts.

**Table 1.** Comparative results for photocatalytic H<sub>2</sub> evolution based on previous reports using TiO<sub>2</sub> or CeO<sub>2</sub>-based photocatalysts in the literature.

| Photocatalyst   | Irradiation Condition                    | Additive        | Rate of H <sub>2</sub> Production         | Ref.      |
|---|--|-----------------|---|-----------|
| N-CeO <sub>2</sub> -x/g-C <sub>3</sub> N <sub>4</sub>           | Xe lamp (300 W)<br>$\lambda > 420$ nm    | Methanol        | 43 $\mu\text{mol h}^{-1} \text{g}^{-1}$   | [32]      |
| MoSe <sub>2</sub> /TiO <sub>2</sub>                             | Xe lamp (300 W)<br>$\lambda > 420$ nm    | Methanol        | 5.14 $\mu\text{mol h}^{-1}$               | [33]      |
| Co <sub>3</sub> O <sub>4</sub> quantum dots on TiO <sub>2</sub> | Xe lamp (300 W)<br>1.5 AM filter         | Methanol        | 41.8 $\mu\text{mol h}^{-1} \text{g}^{-1}$ | [34]      |
| N doped La/TiO <sub>2</sub>                                     | Mercury lamp (8 W)<br>$\lambda > 365$ nm | Methanol        | 8.25 $\mu\text{mol h}^{-1} \text{g}^{-1}$ | [35]      |
| BCN-TiO <sub>2</sub>  | Xe lamp (300 W)<br>$\lambda > 420$ nm    | Triethanolamine | 68.5 $\mu\text{mol h}^{-1} \text{g}^{-1}$ | [36]      |
| Rh-TiO <sub>2</sub> -CeO <sub>2</sub>                           | Xe lamp (300 W)<br>$\lambda > 400$ nm    | Methanol        | 48.3 $\mu\text{mol h}^{-1} \text{g}^{-1}$ | This Work |

The photocatalytic stability for the hydrogen production reaction was further estimated with Rh-TiO<sub>2</sub>-CeO<sub>2</sub> hybrid photocatalysts. To confirm the photocatalytic stabilities of the Rh-TiO<sub>2</sub>-CeO<sub>2</sub> hybrid photocatalysts, their hydrogen production rates were examined by three cycles of repeated hydrogen production reactions under standard conditions. The Rh-TiO<sub>2</sub>-CeO<sub>2</sub> hybrid photocatalysts exhibited nearly retained hydrogen production activity over three repeated photocatalysis cycles (Figure 7c), which indicates the good recyclability of the catalysts.

To unveil the superior photocatalytic activity of Rh-TiO<sub>2</sub>-CeO<sub>2</sub> hybrid photocatalysts compared to the Rh-TiO<sub>2</sub> hybrid and TiO<sub>2</sub> catalysts, photocurrent responses of different photocatalysts were measured to estimate their charge generation and transfer rates (Figure 7d). The Rh-TiO<sub>2</sub>-CeO<sub>2</sub> hybrid photocatalysts showed higher photocurrent density compared to that of the Rh-TiO<sub>2</sub> hybrid and TiO<sub>2</sub> catalysts, demonstrating that the CeO<sub>2</sub> and Rh can improve the separation of photo-induced electron-hole pairs. Furthermore, photoluminescence (PL) measurement performed for investigating the electron transfer process revealed that significant quenching of PL is observed after a combination of CeO<sub>2</sub>

and Rh into TiO<sub>2</sub> (Figure 7e). In addition, compared with TiO<sub>2</sub> catalysts, Rh–TiO<sub>2</sub> hybrid photocatalysts exhibited higher current density (Figure 7d) and lower PL intensity (Figure 7e), respectively. These findings verify that the recombination of electron–hole pairs is effectively suppressed by incorporating both CeO<sub>2</sub> and Rh components. On the other hand, to further investigate the benefit of the Rh domain as a co-catalyst, an electrochemical hydrogen evolution reaction (HER) was performed with different samples (Figure 7f). In HER polarization curves, the potentials are  $-0.28$ ,  $-0.34$ , and  $-0.51$  V vs. RHE at  $10 \text{ mA cm}^{-2}$  for the Rh–TiO<sub>2</sub>–CeO<sub>2</sub> hybrid, Rh–TiO<sub>2</sub> hybrid, and TiO<sub>2</sub> photocatalysts, respectively. This result indicates that the Rh domain promotes the proton reduction to hydrogen. Particularly, the higher HER activity of Rh–TiO<sub>2</sub>–CeO<sub>2</sub> hybrid photocatalysts than Rh–TiO<sub>2</sub> hybrid photocatalysts signifies the promotion effect by the Rh–CeO<sub>2</sub> combination.

### 3. Materials and Methods

#### 3.1. Chemicals

RhCl<sub>3</sub> (rhodium(III) chloride, 98%, Sigma-Aldrich), Ce(NO<sub>3</sub>)<sub>3</sub>·6H<sub>2</sub>O (cerium(III) nitrate hexahydrate, 99.99% trace metals basis, Sigma-Aldrich), urea (NH<sub>2</sub>CONH<sub>2</sub>, 99.0%, Samchun chemical), and TiO<sub>2</sub> (titanium(IV) oxide, anatase, powder, 99.8% trace metals basis, Sigma-Aldrich) were used as received. Deionized water (18.2 MΩ·cm) was used to prepare the reaction mixtures.

#### 3.2. Preparation of Rh–TiO<sub>2</sub>–CeO<sub>2</sub> and Rh–TiO<sub>2</sub> Hybrid Photocatalysts

In a typical preparation of Rh–TiO<sub>2</sub>–CeO<sub>2</sub> hybrid photocatalysts, 2.0 g of urea and 0.5 g of TiO<sub>2</sub> powder were dispersed in 8.0 mL of deionized water. The mixtures were sonicated for 30 min. Then, 10 mL of an aqueous mixture containing 0.967 mmol of Ce(NO<sub>3</sub>)<sub>3</sub>·6H<sub>2</sub>O and 0.165 mmol of RhCl<sub>3</sub> was added to the above mixture with vigorous stirring. The resultant mixture was heated to 95 °C and kept at 95 °C for 24 h with vigorous stirring. Subsequently, wet precipitate was collected by centrifugation and washed two times with deionized water. Then, the wet precipitate was dried at 150 °C for 6 h and finally was calcined at 500 °C in air for 2 h.

For the preparation of Rh–TiO<sub>2</sub> hybrid photocatalysts, all synthetic conditions are identical except adding Ce(NO<sub>3</sub>)<sub>3</sub>·6H<sub>2</sub>O.

#### 3.3. Characterization

DRS was measured with a UV–Vis absorption spectrometer (Shimadzu UV-2600). TEM and EDS elemental mapping images were obtained with a JEOL JEM-2100F transmission electron microscope operating 200 kV after placing a drop of hydrosol on carbon-coated Cu grids (200 mesh). XRD patterns were obtained with a Bruker AXS D8 DISCOVER diffractometer using Cu Kα (0.1542 nm) radiation for 2θ at 20 to 80°. XPS measurements were conducted using a Thermo VG Scientific Thermo VG Scientific Sigma Probe spectrometer with Al Kα X-ray (1486.6 eV). XPS data were calibrated using the C 1s peak at 284.5 eV. PL measurements were performed using an aqueous photocatalyst mixture (1 mg mL<sup>-1</sup>) with Horiba Fluoromax-4. Photocurrent responses and electrochemical HER were conducted in a three-electrode cell using potentiostat (CHI 600E). Ag/AgCl (NaCl 3 M) and Pt wire were used as the reference and counter electrodes, respectively. For measurement of photocurrent responses for photocatalysts, photocatalysts (5 mg) loaded on FTO were irradiated under visible light (λ > 400 nm) using a Xe lamp (300 W, Newport 66902). For electrochemical HER, 100 μg of photocatalysts was loaded on glassy carbon electrode (Diameter size: 5 mm). The linear sweep voltammetry (LSV) measurements were performed in the range potentials from  $-0.6$  to  $0.2$  V (vs. RHE) with a sweep rate of  $5 \text{ mV s}^{-1}$ .

### 3.4. Photocatalysis Experiments

Photocatalytic hydrogen production was performed under visible light irradiation using a Xe lamp (300 W, Newport 66902) and a UV-cut on filter ( $\lambda > 400$  nm). The intensity of light in the cell was measured to be  $100 \text{ mW cm}^{-2}$ . For photocatalytic hydrogen production experiments, 1.0 mg of photocatalysts was dispersed into 20 mL of methanol/deionized water (3/1) mixture. The amount of hydrogen produced during photocatalysis was detected using gas chromatography (GC, Agilent Technologies 7890B).

### 4. Conclusions

In summary, an efficient synthetic method for the preparation of ternary Rh–TiO<sub>2</sub>–CeO<sub>2</sub> photocatalysts with small size and a high distribution of Rh NCs on binary TiO<sub>2</sub>–CeO<sub>2</sub> photocatalysts was developed in this work. The Rh–TiO<sub>2</sub>–CeO<sub>2</sub> hybrid photocatalysts showed extended light absorption compared to the TiO<sub>2</sub>–CeO<sub>2</sub> hybrid and TiO<sub>2</sub> photocatalysts. This improved photocatalytic activity can be ascribed to the synergistic combination of Rh, TiO<sub>2</sub>, and CeO<sub>2</sub>. It is expected that the present strategy will be valuable toward the development of advanced photocatalysts for hydrogen production reactions, and this design can be extended to semiconductor–metal hybrid catalysts with distinct functions.

**Funding:** This work was supported by a National Research Foundation of Korea (NRF) grant (NRF-2020R1C1C1008514) and the Priority Research Centers Program through the National Research Foundation of Korea (NRF) funded by the Ministry of Education, Science and Technology (NRF-2019R1A6A1A11053838).

**Conflicts of Interest:** The authors declare no conflict of interest.

### References

1. Cheng, L.; Xiang, Q.; Liao, Y.; Zhang, H. CdS-based photocatalysts. *Energy Environ. Sci.* **2018**, *11*, 1362–1391. [[CrossRef](#)]
2. Kudo, A.; Miseki, Y. Heterogeneous photocatalyst materials for water splitting. *Chem. Soc. Rev.* **2009**, *38*, 253–278. [[CrossRef](#)] [[PubMed](#)]
3. Wu, H.; Tan, H.L.; Toe, C.Y.; Scott, J.; Wang, L.; Amal, R.; Ng, Y.H. Photocatalytic and photoelectrochemical systems: Similarities and differences. *Adv. Mater.* **2020**, *32*, 1904717. [[CrossRef](#)] [[PubMed](#)]
4. Xu, Q.; Zhang, L.; Yu, J.; Wageh, S.; Al-Ghamdi, A.A.; Jaroniec, M. Direct Z-scheme photocatalysts: Principles, synthesis, and applications. *Mater. Today* **2018**, *21*, 1042–1063. [[CrossRef](#)]
5. Hong, J.W.; Wi, D.H.; Lee, S.-U.; Han, S.W. Metal–semiconductor heteronanostructures with desired configurations for plasmonic photocatalysis. *J. Am. Chem. Soc.* **2016**, *138*, 15766–15773. [[CrossRef](#)]
6. Yu, E.-J.; Kim, H.C.; Kim, H.J.; Jung, S.-Y.; Ryu, K.-S.; Choi, S.-I.; Hong, J.W. Anisotropic heteronanostructures of Cu<sub>2</sub>O–2D MoS<sub>2</sub> for efficient visible light driven photocatalysis. *Appl. Surf. Sci.* **2021**, *538*, 148159. [[CrossRef](#)]
7. Bang, J.; Das, S.; Yu, E.-J.; Kim, K.; Lim, H.; Kim, S.; Hong, J.W. Controlled photoinduced electron transfer from InP/ZnS quantum dots through Cu doping: A new prototype for the visible-light photocatalytic hydrogen evolution reaction. *Nano Lett.* **2020**, *20*, 6263–6271. [[CrossRef](#)]
8. Huang, H.; Dai, B.; Wang, W.; Lu, C.; Kou, J.; Ni, Y.; Wang, L.; Xu, Z. Oriented built-in electric field introduced by surface gradient diffusion doping for enhanced photocatalytic H<sub>2</sub> evolution in CdS nanorods. *Nano Lett.* **2017**, *17*, 3803–3808. [[CrossRef](#)]
9. Liu, N.; Schneider, C.; Freitag, D.; Hartmann, M.; Venkatesan, U.; Müller, J.; Spiecker, E.; Schmuki, P. Black TiO<sub>2</sub> nanotubes: Cocatalyst-free open-circuit hydrogen generation. *Nano Lett.* **2014**, *14*, 3309–3313. [[CrossRef](#)]
10. Ju, L.; Qin, J.; Shi, L.; Yang, G.; Zhang, J.; Sun, L. Rolling the WSe<sub>2</sub> Bilayer into double-walled nanotube for the enhanced photocatalytic water-splitting performance. *Nanomaterials* **2021**, *11*, 705. [[CrossRef](#)]
11. Li, C.; Koenigsmann, C.; Ding, W.; Rudshiteyn, B.; Yang, K.R.; Regan, K.P.; Konezny, S.J.; Batista, V.S.; Brudvig, G.W.; Schmuttermaier, C.A. Facet-dependent photoelectrochemical performance of TiO<sub>2</sub> nanostructures: An experimental and computational study. *J. Am. Chem. Soc.* **2015**, *137*, 1520–1529. [[CrossRef](#)]
12. Kargar, A.; Jing, Y.; Kim, S.J.; Riley, C.T.; Pan, X.; Wang, D. ZnO/CuO heterojunction branched nanowires for photoelectrochemical hydrogen generation. *ACS Nano* **2013**, *7*, 11112–11120. [[CrossRef](#)] [[PubMed](#)]
13. Qiu, B.; Zhu, Q.; Du, M.; Fan, L.; Xing, M.; Zhang, J. Efficient solar light harvesting CdS/Co<sub>9</sub>S<sub>8</sub> hollow cubes for Z-scheme photocatalytic water splitting. *Angew. Chem. Int. Ed.* **2017**, *56*, 2684–2688. [[CrossRef](#)]
14. Mansingh, S.; Padhi, D.; Parida, K. Enhanced photocatalytic activity of nanostructured Fe doped CeO<sub>2</sub> for hydrogen production under visible light irradiation. *Int. J. Hydrog. Energy* **2016**, *41*, 14133–14146. [[CrossRef](#)]
15. Wi, D.H.; Park, S.Y.; Lee, S.; Sung, J.; Hong, J.W.; Han, S.W. Metal–semiconductor ternary hybrids for efficient visible-light photocatalytic hydrogen evolution. *J. Mater. Chem. A* **2018**, *6*, 13225–13235. [[CrossRef](#)]

16. Sun, B.; Zhou, W.; Li, H.; Ren, L.; Qiao, P.; Li, W.; Fu, H. Synthesis of particulate hierarchical tandem heterojunctions toward optimized photocatalytic hydrogen production. *Adv. Mater.* **2018**, *30*, 1804282. [[CrossRef](#)] [[PubMed](#)]
17. Tan, C.F.; Su, A.K.; Chen, Z.; Liow, C.H.; Phan, H.T.; Tan, H.R.; Xu, Q.-H.; Ho, G.W. Inverse stellation of CuAu-ZnO multimetallic-semiconductor nanostartube for plasmon-enhanced photocatalysis. *ACS Nano* **2018**, *12*, 4512–4520. [[CrossRef](#)] [[PubMed](#)]
18. Wang, Q.; Hisatomi, T.; Jia, Q.; Tokudome, H.; Zhong, M.; Wang, C.; Pan, Z.; Takata, T.; Nakabayashi, M.; Shibata, N. Scalable water splitting on particulate photocatalyst sheets with a solar-to-hydrogen energy conversion efficiency exceeding 1%. *Nat. Mater.* **2016**, *15*, 611–615. [[CrossRef](#)] [[PubMed](#)]
19. Kang, Y.; Ye, X.; Murray, C.B. Size- and shape-selective synthesis of metal nanocrystals and nanowires using CO as a reducing agent. *Angew. Chem. Int. Ed.* **2010**, *49*, 6156–6159. [[CrossRef](#)]
20. Qian, K.; Sweeny, B.C.; Johnston-Peck, A.C.; Niu, W.; Graham, J.O.; DuChene, J.S.; Qiu, J.; Wang, Y.-C.; Engelhard, M.H.; Su, D. Surface plasmon-driven water reduction: Gold nanoparticle size matters. *J. Am. Chem. Soc.* **2014**, *136*, 9842–9845. [[CrossRef](#)]
21. Ramasamy, K.; Malik, M.A.; Revaprasadu, N.; O'Brien, P. Routes to nanostructured inorganic materials with potential for solar energy applications. *Chem. Mater.* **2013**, *25*, 3551–3569. [[CrossRef](#)]
22. Nakibli, Y.; Mazal, Y.; Dubi, Y.; Wächtler, M.; Amirav, L. Size matters: Cocatalyst size effect on charge transfer and photocatalytic activity. *Nano Lett.* **2018**, *18*, 357–364. [[CrossRef](#)] [[PubMed](#)]
23. Wolff, C.M.; Frischmann, P.D.; Schulze, M.; Bohn, B.J.; Wein, R.; Livadas, P.; Carlson, M.T.; Jäckel, F.; Feldmann, J.; Würthner, F. All-in-one visible-light-driven water splitting by combining nanoparticulate and molecular co-catalysts on CdS nanorods. *Nat. Energy* **2018**, *3*, 862–869. [[CrossRef](#)]
24. Zhao, Y.; Min, X.; Ding, Z.; Chen, S.; Ai, C.; Liu, Z.; Yang, T.; Wu, X.; Liu, Y.; Lin, S.; et al. Metal-based nanocatalysts via a universal design on cellular structure. *Adv. Sci.* **2020**, *7*, 1902051. [[CrossRef](#)] [[PubMed](#)]
25. Chen, X.; Shen, S.; Guo, L.; Mao, S.S. Semiconductor-based photocatalytic hydrogen generation. *Chem. Rev.* **2010**, *110*, 6503–6570. [[CrossRef](#)] [[PubMed](#)]
26. Gao, X.; Wu, H.B.; Zheng, L.; Zhong, Y.; Hu, Y.; Lou, X.W. Formation of mesoporous heterostructured BiVO<sub>4</sub>/Bi<sub>2</sub>S<sub>3</sub> hollow discoids with enhanced photoactivity. *Angew. Chem. Int. Ed.* **2014**, *53*, 5917–5921. [[CrossRef](#)]
27. Linic, S.; Christopher, P.; Ingram, D.B. Plasmonic-metal nanostructures for efficient conversion of solar to chemical energy. *Nat. Mater.* **2011**, *10*, 911–921. [[CrossRef](#)]
28. Eskandarloo, H.; Badii, A.; Behnajady, M.A. TiO<sub>2</sub>/CeO<sub>2</sub> Hybrid photocatalyst with enhanced photocatalytic activity: Optimization of synthesis variables. *Ind. Eng. Chem. Res.* **2014**, *53*, 7847–7855. [[CrossRef](#)]
29. Lu, X.; Li, X.; Chen, F.; Chen, Z.; Qian, J.; Zhang, Q. Biotemplating synthesis of N-doped two-dimensional CeO<sub>2</sub>-TiO<sub>2</sub> nanosheets with enhanced visible light photocatalytic desulfurization performance. *J. Alloys Compd.* **2020**, *815*, 152326. [[CrossRef](#)]
30. Luo, F.; Guo, L.; Xie, Y.; Xu, J.; Cai, W.; Qu, K.; Yang, Z. Robust hydrogen evolution reaction activity catalyzed by ultrasmall Rh-Rh<sub>2</sub>P nanoparticles. *J. Mater. Chem. A* **2020**, *8*, 12378–12384. [[CrossRef](#)]
31. Soldano, G.; Schulz, E.N.; Salinas, D.R.; Santos, E.; Schmickler, W. Hydrogen electrocatalysis on overlayers of rhodium over gold and palladium substrates—More active than platinum? *Phys. Chem. Chem. Phys.* **2011**, *13*, 16437–16443. [[CrossRef](#)]
32. Waqas, M.; Yang, B.; Cao, L.; Zhao, X.; Iqbal, W.; Xiao, K.; Zhu, C.; Zhang, J. Tuning the N-bonded cerium(III) fraction/g-C<sub>3</sub>N<sub>4</sub> interface in hollow structures using an in situ reduction treatment for superior photochemical hydrogen evolution. *Catal. Sci. Technol.* **2019**, *9*, 5322–5332.
33. Wu, L.; Shi, S.; Li, Q.; Zhang, X.; Cui, X. TiO<sub>2</sub> nanoparticles modified with 2D MoSe<sub>2</sub> for enhanced photocatalytic activity on hydrogen evolution. *Int. J. Hydrog. Energy* **2019**, *44*, 720–728. [[CrossRef](#)]
34. Liu, J.; Ke, J.; Li, Y.; Liu, B.J.; Wang, L.D.; Xiao, H.N.; Wang, S.B. Co<sub>3</sub>O<sub>4</sub> quantum dots/TiO<sub>2</sub> nanobelt hybrids for highly efficient photocatalytic overall water splitting. *Appl. Catal. B-Environ.* **2018**, *236*, 396–403. [[CrossRef](#)]
35. Dubnova, L.; Zvolkska, M.; Edelmanna, M.; Matejova, L.; Reli, M.; Drobna, H.; Kustrowski, P.; Koci, K.; Capek, L. Photocatalytic decomposition of methanol-water solution over N-La/TiO<sub>2</sub> photocatalysts. *Appl. Surf. Sci.* **2019**, *469*, 879–886. [[CrossRef](#)]
36. Xing, X.; Zhu, H.; Zhang, M.; Xiao, L.; Li, Q.; Yang, J. Effect of heterojunctions and phase-junctions on visible-light photocatalytic hydrogen evolution in BCN-TiO<sub>2</sub> photocatalysts. *Chem. Phys. Lett.* **2019**, *727*, 11–18. [[CrossRef](#)]